IEEE Access
Multidisciplinary | Rapid Review | Open Access Journal

Received March 20, 2020, accepted April 9, 2020, date of publication April 22, 2020, date of current version May 6, 2020.

Digital Object Identifier 10.1109/ACCESS.2020.2989378

Hovering Control of Submersible Transformer Inspection Robot Based on ASMBC Method

YINGBIN FENG[1], YANJU LIU[1], HONGWEI GAO[1], AND ZHAOJIE JU[2], (Senior Member, IEEE)
[1]School of Automation and Electrical Engineering, Shenyang Ligong University, Shenyang 110159, China
[2]School of Computing, University of Portsmouth, Portsmouth PO1 3HE, U.K.

Corresponding authors: Yanju Liu (6133292@qq.com) and Zhaojie Ju (author@ boulder.nist.gov).

This work was supported in part by the China Postdoctoral Science Foundation under Grant 2019M661127, in part by the Natural Science Foundation of Liaoning Province under Grant 2019-ZD-0250, and in part by the National Natural Science Foundation of China under Grant 51575412.

ABSTRACT Aiming at the difficulty in locating and identifying the faults of oil-immersed transformers, a new spherical submersible transformer inspection robot is designed. The robot has a spherical structure with a zero turn radius, which ensures its flexible motion. It is a difficult problem for the underactuated spherical robot to realize the hovering control for identifying transformer fault points. To address the problem, the dynamic model and kinematics equations of the robot are derived by the hydrodynamic theory at first. Then, an adaptive sliding mode backstepping control (ASMBC) is used to design the cascade control system. The cascade control system consists of the depth control and the yaw control. The performance of the controller is verified by both simulation and real experiments. The simulation experimental results demonstrate that ASMBC controller is superior to the single neuron PID. The tank trials results show that the movement of the robot is flexible, and the hover control can satisfy the requirement of fault observation tasks.

INDEX TERMS Oil-immersed transformer, robot, dynamic model, sliding mode backstepping control.

I. INTRODUCTION

The safe and stable operation of power system is important for people's daily life. As one of the transfer station, transformers has been widely used in power systems. The reliability and performance of transformers play a crucial role in the normal operation of power system [1], [2]. Therefore, in the process of power system operation and maintenance, how to identify and locate the internal fault of transformer efficiently, timely and accurately is great significance to the stable operation of the power system.

At present, methods for transformer fault detection are proposed mainly based on the characteristic signal of transformer status. They can be divided into many classes, including the chromatographic technique [3], [4], the infrared spectrum technology [5], the sensor array online detection technology and transformer oil temperature detection technology [6], and so on. With the development of artificial intelligence technology, many artificial intelligent comprehensive fault diagnosis methods have been presented based on neural network [7], expert system [8], support vector machine [9], frequency response analysis [10], etc. However, the above methods are indirect fault diagnosis, which cannot provide an accurate fault location. To solve this problem, all transformer oil should be completely drained and the maintenance personnel should enter the transformer during each inspection. However, manual inspection method has many problems, such as high risk, low efficiency, and secondary pollution.

In 2018, ABB firstly introduced the oil-immersed transformer internal inspection robot, which is named TXplore robot [11], [12]. The TXplore robot is equipped with multiple cameras. The shape of the robot is rectangular with size of 18*20*24cm. TXplore robot is derived by four propellers, which are the common driving method of Autonomous Underwater Vehicle (AUV). Therefore, it can complete the internal inspection of the transformer structure without releasing the oil. However, when the propeller rotates at high speed, it is easy to generate bubbles that reduce dielectric strength of transformer oil [13]. In addition, the turn radius of TXplore Robot is big, which is difficult for the robot to move flexibly inside the transformer.

There has been less research on robot working in transformer oil. In the design of the robot, we refer to the underwater vehicles that play crucial roles in different

The associate editor coordinating the review of this manuscript and approving it for publication was Okyay Kaynak.

application areas [14]. Specific applications include marine resource exploration, national security, and search and rescue in hazardous environments. Different applications or tasks require different shapes, sizes and configurations of AUVs. However, these conventional AUVs are not able to carry out detailed inspection tasks at zero or slow forward speeds in a narrow space [15]. Therefore, numerous scholars have carried out research on underwater robots with spherical structures. An autonomous underwater spherical robot ODIN with six degree of freedom has been designed at the University of Hawaii [16]. For testing various kinds of algorithms, Choi H.T. et al proposed a spherical AUV named ODINIII with eight thrusters, which could provide instantaneous and omnidirectional prowess [17]. A new-type spherical underwater vehicle BYSQ-2 was provided in paper [18]. BYSQ-2 could complete 6 degrees of freedom (6-DOF) movement by a thruster and a steering gear with a dual drive. Based on the motion analysis, the dynamics model of BYQ-3 spherical robot was established by Kane equation modeling method [19]. A finite-time stabilization controller was put forward for BYQ-3, which could ensure robot stated converge to zero in finite time [20]. In order to study the motion performance of a spherical robot based on vectored water-jet propulsion system, Yue C. et al designed a spherical underwater robot (SURII) with complex water-jet propulsion system [21]. The propulsion system included three water-jet thrusters and six servomotors. A novel propulsion system for SURIII was devised [22]. The experiment results demonstrate the propulsive force of the propulsion system is better than SURII. The Eyeball ROV has been designed in paper [23], which can move in any direction by a pair of thrusters. Considering the complex of underwater spherical robot, a neural network-based auto-turning control system was designed. The neural network can automatically estimate the suitable set of control gains [24].

It is difficult problem for AUV to hover at zero speeds. Various methods have been advanced for hovering of AUV. Steenson L. V. designed a hover-capable AUV with four through-body tunnel thrusters and a rear propeller. A PI-D based control system was developed to enable a smooth transition from hover-style to flight-style operation of AUV [15]. Varying the vehicle buoyancy and attitude was used to control the depth of AUV [16]. In order to improve the depth tracking control performance of under actuated AUV, an adaptive backstepping controller based on a nonlinear disturbance observer was proposed [27].

We refer to structure of underwater robot in paper [17], [21], and design a new spherical submersible transformer inspection robot (SSTIR) with six oil-jet thrusters in this paper. The SSTIR has a small size, zero turn radius and can achieve 4 degrees of freedom movement in the transformer oil. Although the SSTIR is fitted with two oil-jet thrusters in the vertical plane, the oil-jet thrusters provide only force on the robot in the downward direction. The SSTIR should have slightly positively buoyant, allowing the vehicle to move in the upward direction. Moreover, the SSTIR can float to the oil surface in the event system failure. If the SSTIR hovers in the transformer oil, two oil-jet thrusters in vertical plane work all the time to overcome the positive buoyancy. Due to the robot with spherical hull, the oil resistance is very small in the yaw direction. The environmental disturbance from two oil-jet thrusters working will cause the robot yawing motion. Therefore, it is a difficult problem for the under-actuated spherical robot to realize hovering control for identifying transformer fault points. In order to solve this problem, the dynamic model for the robot is obtained by the hydrodynamic theory. Afterwards, the cascade control system is put forward for hover-style operation of the robot. The cascade control system includes the depth control and the yaw control. An adaptive sliding mode backstepping controller based on self-learning is developed for the depth control. The self-learning controller is used to counteract the positive buoyancy of the SSTIR, which can reduce the setting time of the adaptive sliding mode backstepping controller. And an adaptive sliding mode backstepping controller is designed for the heading control. Since the environmental disturbance from the depth control is time-varying, an adaptive sliding mode backsteeping controller can adjust control parameters to adapt to environmental disturbance.

The rest of the paper is organized as follows. In Section II, the mechanical structure of transformer is described. In Section III, the mechanical structure and control system of robot are designed. Section IV gives the dynamic model and kinematics equations of the SSTIR. Section V demonstrates the hovering control method of the SSTIR. A series of experiments are used to illustrate the feasibility of the SSTIR in section VI and VII. Finally, some conclusions are made in Section VIII.

II. STRUCTURE OF OIL-IMMERSED TRANSFORMER

In order to design the robot, we need to understand the structure of oil-immersed transformer. The structure of three-phase transformer (510cm×230cm×350cm) mainly consists of oil tank, core, winding, bushing, cooler, manhole, and conservator, as shown in Fig. 1 [28]. There are a large number of lock nuts, screws and cables in the oil-immersed transformer, which may interfere with the robot motion. The oil tank is filled with the 25# transformer oil that is mainly used for insulation, heat dissipation and arc extinction.

The top view of the oil-immersed transformer is shown in Fig. 2. As can be seen from Fig. 2, the core and winding are located in the center of the oil tank, and the shortest distance between the winding and the inner wall of oil tank is only 25cm. Therefore, the maximum size of the robot should be less than 25cm. Manhole with 40cm diameter is located on the top of the transformer. The robot enters the transformer through the manhole. The dashed red line indicates the observation track of the robot inside the transformer. The robot detects winding faults along the red track at different depths. L_A, L_B, and L_C represent LV bushing, H_A, H_B, and H_C represent HV bushing.

FIGURE 1. Photograph of three-phase oil-immersed transformer.

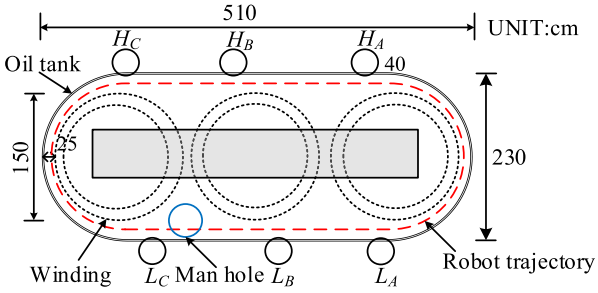

FIGURE 2. Top view of the oil-immersed transformer.

Based on the above analysis, the following factors need to be considered for designing the robot:

(i) The oil tank is filled with the 25# transformer oil, so the robot should be protected from transformer oil corrosion.

(ii) The narrow and complex transformer internal structure requires the robot to have flexible motion.

(iii) The dynamic model of robot in transformer oil needs to be analyzed.

III. THE SSTIR SYSTEM DESIGN

A. MECHANICAL DESIGN OF THE SSTIR

Because the working environment of the SSTIR is different from the previous AUV, mechanical structure of the SSTIR differs from previous spherical AUV. There are various ways to design robot structure, which are typically specific to the task and environment. According to robot task and environment, we give some mechanical design considerations, required pressure or depth, operating temperature range, size requirements, transformer oil corrosion.

1) STRUCTURE OF THE SSTIR

The height of 220kV oil-immersed transformer is generally less than 5 m. The SSTIR hull should bear the pressure at a transformer oil depth of at least 5 m. The temperature of transformer oil can reach 70-80 degree Celsius during transformer operation. Therefore, when the robot performs fault detection task the transformer must stop working. The working temperature of the SSTIR is about 0-40 degree Celsius. The subsection II gives that the narrowest space inside the transformer is only 25cm. The SSTIR is 19cm in diameter, and can pass through the narrowest space.

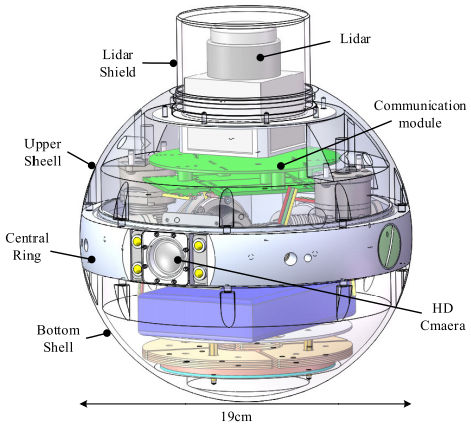

FIGURE 3. Outline structure of robot.

The spherical structure has the two advantages: zero turning radius, flexible movement. To guarantee the robot can move in the narrow space filled with transformer oil, the robot is designed with a completely closed spherical structure. The SSTIR hull consists of Lidar hull, Upper hull, Bottom hull and central ring, as show in Fig. 3. The four parts are connected with waterproof hermetic O-rings. The Lidar hull, Upper hull and Bottom hull are made of polycarbonate, which has good resistance to transformer oil corrosion [29]. The central ring is made of 6061 aluminum alloy, which is resistant to transformer oil corrosion and helpful for the internal heat exchanging.

2) PROPULSION SYSTEM OF THE SSTIR

The blade thruster with excellent performance is widely used in propulsion system of AUV [30]. However, it is well known that the blade thruster will generate bubbles at high speed rotating. A lot of bubbles will reduce dielectric strength of transformer oil [13]. Consequently, we adopt oil-jet thruster for the propulsion system of the SSTIR. In order to ensure that the robot has the ability to move flexibly in multiple degrees of freedom (MDOF), four oil-jet thrusters are designed in the central ring of the robot. Eight holes were cut into the central ring for the thruster inlet and outlet nozzles. The oil-jet thruster is directly connected inlet and outlet nozzles, and the O-ring sealing is pressed between the end faces of the flange and central ring, as shown in Fig. 4. The oil-jet thruster arrangement enables the robot to move with 3 DOF including yaw motion, surge motion and sway motion. Two oil-jet thrusters are designed in the vertical plane to enable the robot in heave motion. Since the oil-jet thruster cannot change injection direction, the vertical oil-jet thruster need to be closed while the robot moves in upward direction by positive buoyancy. The propulsion system layout is shown in Fig. 5.

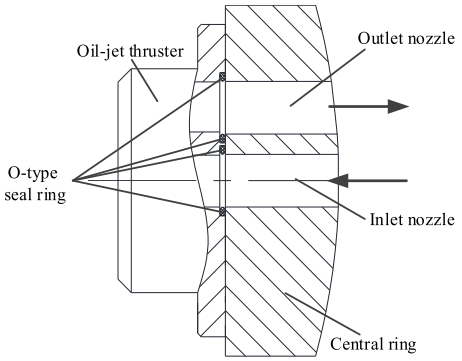

FIGURE 4. Oil-jet thruster seal structure.

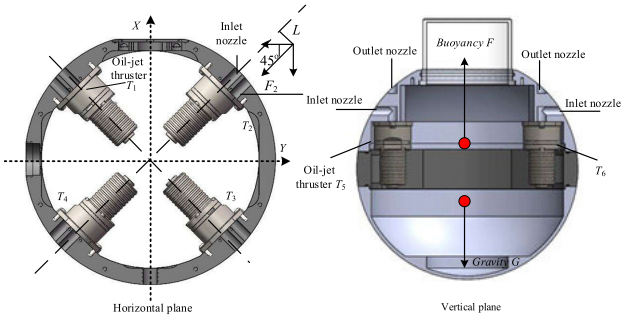

FIGURE 5. Propulsion system layout.

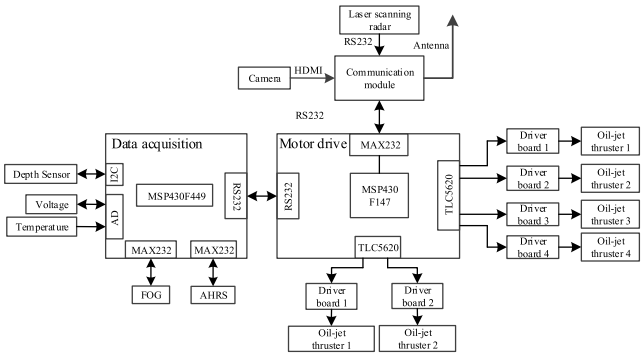

FIGURE 6. Control circuit of the SSTIR.

B. THE SSTIR CONTROL SYSTEM DESIGN

1) STRUCTURE OF CONTROL SYSTEM

The hardware architecture of the SSTIR control system is shown in Fig. 6, including observation and communication system, motion control system, and data acquisition system. RS232 is used for data transmission between different systems. The observation and communication system consists of HD camera, Lidar and Wireless communication module. Wireless communication protects robot movement from communication cable. The SSTIR can move more flexibly. Moreover, the Lidar provides the horizontal position of the robot inside the transformer and detects the obstacle around the robot. HD camera is used to observe faults. The communication module can simultaneously transmit HD camera, Lidar data and control command to robot remote control

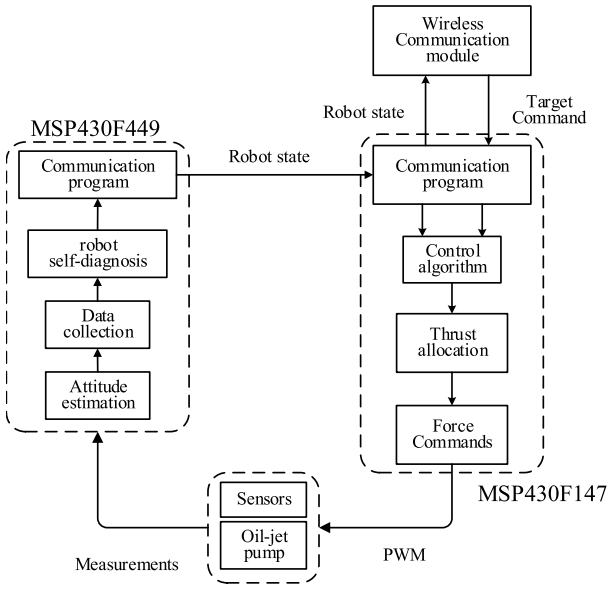

FIGURE 7. Software system of the SSTIR.

system. The motion control system consists of microprocessor unit (MSP430F147), driver board and oil-jet thruster. The motion control system realizes instruction transmission, control algorithm, thrust allocation. Analog voltage signals is used for propeller speed to adjust the propulsive forces of the thrusters. MSP430F147 provides six analog voltage channels, which are used to control six oil-jet thrusters separately. The data acquisition system consists of microprocessor unit (MSP430F449), Single-axis fiber optic gyroscope (Single-axis FOG), attitude and heading reference system (AHRS), depth gauge, thermometer, and voltage sensor. The interfaces between the MSP430F449 and those sensors are shown in the Fig. 5. The MSP430F449 receives depth from the depth gauge, yaw angle from Single-aix FOG, attitude information from AHRS, temperature in the hull from thermometer, battery level from voltage sensor.

2) SOFTWARE SYSTEM DESIGN

Since IAR 5.4.2 soft development environment gives comprehensive group of software tools and functional libraries for data acquisition, presentation and analysis [31], which is used for programming for the robot control system. According to the robot control circuit, the robot software is divided into two parts, control program of MSP430F147 and control program of MSP430F449.

As shown in Fig. 7, the software architecture of MSP-430F147 contains of the communication program, control algorithm, thrust allocation, and force Commands. The communication program receives target commands from wireless communication module, the robot state from MSP430F449, and sends various parameters that are needed by control algorithm. Target commands cover expected velocity, depth, and yaw angle of robot. Robot states include depth and yaw angles of the robot in real time, the battery level, temperature

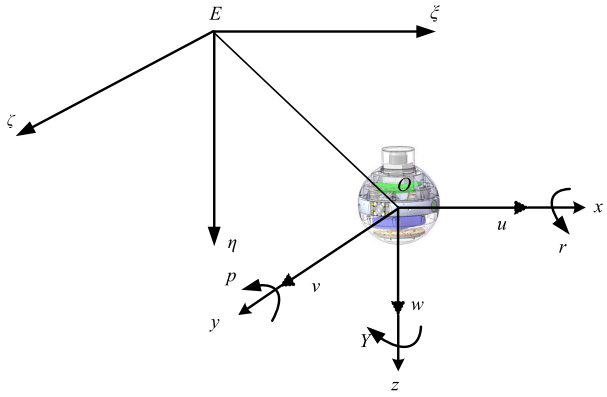

FIGURE 8. The earth-fixed frame and body-fixed frame of robot.

in the hull, and so on. In accordance with preset expected values and real-time data from sensors of robot, the control algorithm calculates the required force to control robot. The control algorithm is the most substantial section of the control system. The thrust allocation produces analog voltage signals and enable signal of oil-jet thruster by the required force from control algorithm. The analog voltage signal is used to control the speed of oil-jet thruster and robot motion. Sensors measure various parameters of the robot motion, which includes robot attitude, depth, and so on. The software architecture of MSP430F449 contains of the communication program, robot self-diagnosis, data collection and attitude estimation. The communication program sends robot state to MSP430F147. The data collection module receives different type of data from sensors. To enhance the robot safety, we designed the robot self-diagnosis module, which judges whether the robot has fault according to the sensors data.

IV. THE SSTIR MODELING

A. DYNAMIC MODEL OF THE SSTIR

It is well know that hydrodynamic theory can be used to analyze the dynamic model of the SSTIR in the transformer oil. In order to study the dynamic model and kinematics model of the SSTIR, two reference frames are considered, the earth-fixed frame $E_{\xi\zeta\eta}$ and the body-fixed frame O_{xyz}, as shown in Fig. 8. The body-fixed frame O_{xyz} is fixed to this robot hull. The center of robot buoyancy is the origin O of the body-fixed frame, the body axes O_x, O_y, and O_z coincide with the principal axes of inertia.

The dynamic model of AUV could be derived from the Newton-Euler equations. Referring to dynamic model of AUV [32], [33], 6-DOF nonlinear equation of the SSTIR is expressed as,

$$(M_{RB} + M_A)\dot{V} + (C_{RB}(V) + C_A(V))V = i + G - D(V)V + W_e \quad (1)$$

where, $V = [u, v, w, p, q, r]^T$, in which u, v, w, p, q and r represent surge, sway, heave, roll, pitch, and yaw velocities. M_{RB} is the rigid body system inertia matrix, M_A is the added mass matrix, $C_{RB}(V)$ is the rigid body Coriolis and centripetal matrix, $C_A(V)$ is the hydrodynamic Coriolis and centripetal matrix, i is a generalized force and moment due to oil-jet thruster, G is vector of gravitational/buoyancy forces and moments, $D(V)$ is the damping matrix, $W_e = [W_u, W_v, W_w, W_p, W_q, W_r]^T$ is vector of environmental disturbances. The environmental disturbances are mainly caused by robot motion.

Before the dynamic model of the SSTIR is analyzed, we give the following assumption,

(i) The center of gravity and the center of buoyancy are located vertically on the O_z-axis. So, the center of gravity in the body-fixed frame is $(0, 0, z_g)$.

(ii) The robot has homogeneous mass distribution, and the robot structure is symmetrical about the Oxz-plane and Oyz-plane and approximate symmetrical about the Oxy-plane. So that, the products of inertia can be expressed as $I_{xy} = I_{yz} = I_{xz} = 0$.

(iii) The maximum speed of this robot is only 0.15m/s, the robot moves at a slow speed.

In this case, the matrices M_{RB} can be expressed as,

$$M_{RB} = \begin{bmatrix} m & 0 & 0 & 0 & mz_g & 0 \\ 0 & m & 0 & -mz_g & 0 & 0 \\ 0 & 0 & m & 0 & 0 & 0 \\ 0 & -mz_g & 0 & I_x & 0 & 0 \\ mz_g & 0 & 0 & 0 & I_y & 0 \\ 0 & 0 & 0 & 0 & 0 & I_z \end{bmatrix} \quad (2)$$

where, m is the mass of this robot, I_x, I_y, I_z are the moments of inertia about the O_x, O_y and O_z axes.

Based the assumption (ii) (iii), we can neglect the contribution from the off-diagonal elements in the added mass matrix M_A [32]. The matrices M_A can be expressed as,

$$M_A = -diag\left\{X_{\dot{u}}, Y_{\dot{v}}, Z_{\dot{w}}, K_{\dot{p}}, M_{\dot{q}}, N_{\dot{r}}\right\} \quad (3)$$

where, $X_{\dot{u}}$, $Y_{\dot{v}}$, $Z_{\dot{w}}$, $K_{\dot{P}}$, $M_{\dot{q}}$,$N_{\dot{r}}$, are the factor of added mass.

Due to the assumption (i) (ii) (iii), the rigid body Coriolis and centripetal matrix$C_{RB}(V)$ would be simplified as [34] (4), as shown at the bottom of the next page,

Due to the assumption (ii) (iii), the hydrodynamic Coriolis and centripetal matrix $C_A(V)$ can be expressed as [32],

$$C_A(V) = \begin{bmatrix} 0 & 0 & 0 & 0 & -Z_{\dot{w}}w & Y_{\dot{v}}v \\ 0 & 0 & 0 & Z_{\dot{w}}w & o & -X_{\dot{u}}u \\ 0 & 0 & 0 & -Y_{\dot{v}}v & X_{\dot{u}}u & 0 \\ 0 & -Z_{\dot{w}}w & Y_{\dot{v}}v & 0 & -N_{\dot{r}}r & M_{\dot{q}}q \\ Z_{\dot{w}}w & 0 & -X_{\dot{u}}u & N_{\dot{r}}r & 0 & K_{\dot{p}}p \\ -Y_{\dot{v}}v & X_{\dot{u}}u & 0 & -M_{\dot{q}}q & K_{\dot{p}}p & 0 \end{bmatrix} \quad (5)$$

In general, the damping force is highly nonlinear and coupled at a high speed. However, based on the assumption (ii) (iii), its terms, higher than the second order can be ignored. A non-coupled with linear and quadratic damping force can be expressed as [35],

$$D(V) = -diag\{X_u + X_{u|u|}|u|, Y_v + Y_{v|v|}|v|,$$

$$Z_w + Z_{w|w|}\,|w|\,, K_p + K_{p|p|}\,|p|\,,$$
$$M_q + M_{q|q|}\,|q|\,, N_r + N_{r|r|}\,|r|\} \tag{6}$$

The generalized forces and moments due to oil-jet thruster i can be expressed as,

$$i = \begin{bmatrix} F_u & F_v & F_w & T_p & T_q & T_r \end{bmatrix}^T \tag{7}$$

where, F_u, F_v, F_w, T_p, T_q and T_r represent the force on the robot in surge, sway, heave, pitch, roll and yaw directions, respectively. According to the installation mode of oil-jet thruster, there is no moment acting on the robot in pitch and roll directions. Therefore, the moments$T_p = T_q = 0$. We can neglect robot movements in pitch and roll direction. Due to the symmetry of the robot, the representation equation F_u is similar withF_v. So, we give only the equation of F_u. When this robot moves forward in the surge direction, F_u is represented as,

$$F_u = (F_3 + F_4)\cos 45^\circ = \frac{\sqrt{2}}{2}(F_3 + F_4) \tag{8}$$

where, F_3 and F_4 represent the reactive force of oil-jet thrusters T_3,T_4 respectively.

Referring to Equ. 8, the forces and moments on the robot in the other direction of the horizontal plane can be easily expressed. When this robot moves downward in the heave direction, T_w is represented as,

$$T_w = F_5 + F_6 \tag{9}$$

where, F_5 and F_6 represent the reactive force of oil-jet thrusters T_5,T_6 respectively. If F_w= 0, the robot moves upward in heave direction by the buoyancy force.

Since the oil-jet thruster cannot provide upward thrust, the robot can only rely on robot buoyancy to move upward. Therefore, the buoyancy force (B) of robot is greater than its gravity (W). Since the center of robot Buoyancy (CB) is the origin O of the body-fixed frame, the coordinates of CB is (0,0,0). In addition, the coordinates of CG is $(0, 0, z_g)$. Consequently, the vector of gravitational/buoyancy forces and moments$g$ is represented as [32],

$$G = \begin{bmatrix} \text{(W-B)}\sin(\theta) \\ -\text{(W-B)}\cos(\theta)\sin(\varphi) \\ -\text{(W-B)}\cos(\theta)\cos(\varphi) \\ z_g W\cos(\theta)\sin(\varphi) \\ z_g W\sin(\theta) \\ 0 \end{bmatrix} \tag{10}$$

where, the weight of the robot is $W = mg$, the buoyancy force of the robot is $B = \rho g V$, g is the acceleration of gravity, ρ is the density of transformer oil, and V is the volume of the robot. θ and φ represent pitch and roll angle respectively. There are just negligible motions in the pitch and roll direction, then $\theta = \varphi \approx 0$. For this case, G will be represented as,

$$G = \begin{bmatrix} 0 \\ 0 \\ B - W \\ 0 \\ 0 \\ 0 \end{bmatrix} \tag{11}$$

Since the movements of robot in the pitch and roll direction can be neglected, $p = q$= 0, the dynamic model of the SSTIR are simplified as,

$$\begin{cases} (m - X_{\dot{u}})\,\dot{u} - (m - Y_{\dot{v}})\,vr + Y_{\dot{v}}vr + \left(X_u + X_{u|u|}\,|u|\right)u = F_u + W_u \\ (m - Y_{\dot{v}})\,\dot{v} + (m - X_{\dot{u}})\,ur + \left(Y_v + Y_{v|v|}\,|v|\right)v = F_v + W_v \\ (m - Z_{\dot{w}})\,\dot{w} + \left(Z_w + Z_{w|w|}\,|w|\right)w = F_w + B - M + W_w \\ (I_z - N_{\dot{r}})\,\dot{r} - Y_{\dot{v}}vu + X_{\dot{u}}uv + \left(N_r + N_{r|r|}\,|r|\right)r = T_r + W_r \end{cases} \tag{12}$$

B. KINEMATICS MODEL OF THE SSTIR

Referring to kinematics model of AUV [36], the kinem-atics model of the SSTIR are described as,

$$\begin{cases} \dot{X} = u\cos(\psi) - v\sin(\psi) \\ \dot{Y} = u\sin(\psi) + v\cos(\psi) \\ \dot{Z} = w \\ \dot{\psi} = r \end{cases} \tag{13}$$

where, $\dot{X}$, $\dot{Y}$, and $\dot{Z}$ are the positions in the E_ξ, E_ζ and E_η axes, respectively. ψ is the rotation angle around the E_η axes in the earth-fixed frame, as shown in Fig. 8.

C. MODELING OF SINGLE OIL-JET THRUSTER

The thrust of oil-jet thruster is related to the angular velocity of motor, the diameter of nozzle, velocity of incoming flow, and so on. In order to establish dynamic modeling of oil-jet thruster, we give the internal structure of the oil-jet pump, as shown in Fig. 9. Where, V_i is velocity of incoming flow, ω is angular velocity of the motor, V_c is the central flow velocity in the nozzle, D is diameter of nozzle, and V_o is velocity of outlet flow. There are four blades, the motor shaft is perpendicular to the nozzle. The internal structure of the oil-jet thruster is similar to that of the water-jet thruster in

$$C_{RB}(V) = \begin{bmatrix} 0 & 0 & 0 & mz_g r & mw & -mv \\ 0 & 0 & 0 & -mw & mz_g r & mu \\ 0 & 0 & 0 & -m\left(z_g p - v\right) & -m\left(z_g q + u\right) & 0 \\ -mz_g r & mw & m\left(z_g p - v\right) & 0 & I_z r & -I_y q \\ -mw & -mz_g r & m\left(z_g q + u\right) & -I_z r & 0 & I_x p \\ mv & -mu & 0 & I_y q & -I_x p & 0 \end{bmatrix} \tag{4}$$

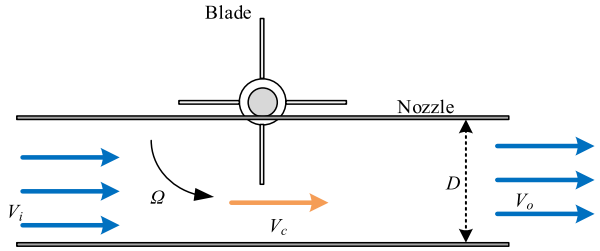

FIGURE 9. The flow model for the internal structure of oil-jet thruster.

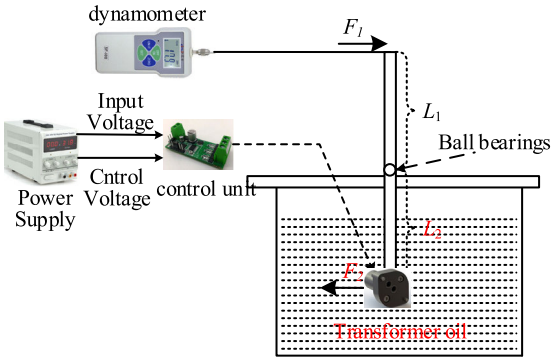

FIGURE 10. The experiment scheme.

paper [37]. With reference to the method in [37], we gives the thrust equation of oil-jet thruster.

$$F = \frac{\pi}{4}\rho D^2\left(k_1^2 V_o^2 + 2k_1k_2V_oD\omega + k_2^2D^2\omega^2\right) \quad (14)$$

$$V_o = k_1V_i + k_2V_c \quad (15)$$

$$V_c = \frac{1}{2}D\omega \quad (16)$$

where, ρ is the density of transformer oil. The velocity of outlet flow V_o is a linear combine of incoming flow velocity and the central flow velocity. $k_1$and k_2 are the proportionality factor. Since unknown parameters k_1,k_2, V_o cannot be obtained by theoretical analysis, we designed an experiment to identify these parameters.

The Equ. (14) shows that the thrust of oil-jet thruster mainly depends on the motor speed. Motor speed is determined by the control voltage and input voltage of the motor. Therefore, the purpose of these experiments is to calculate the relationship between control voltage, input voltage and the thrust of oil-jet thruster. Since general dynamometer is not used in transformer oil, we design the thrust experimental system of oil-jet thruster based on lever principle, as shown in Fig. 10. The experimental system consists of dynamometer, oil-jet thruster, control unit, power supply, transformer oil, and lever with ball bearings. The oil-jet thruster is fixed on the lever, and placed in the transformer oil. The control unit can accept an input voltage range of 10-12V. The control unit can control the flow of oil-jet thruster by a control voltage signal range of 0.7-3.5V.

According to the lever principle, the Equ. (17) is valid.

$$F_1 \times L_1 = F_2 \times L_2 \quad (17)$$

If $L_1 = L_2$, then $F_1 = F_2$.

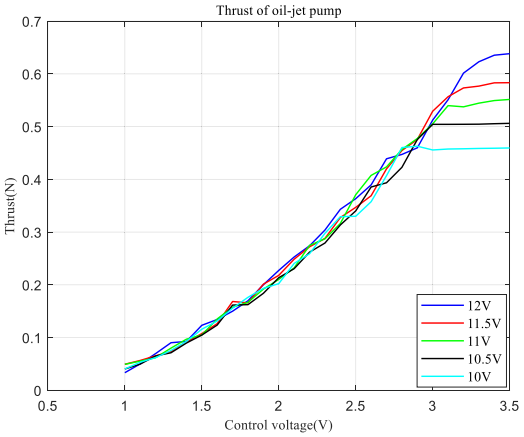

FIGURE 11. The experiment results.

To research oil-jet thruster modeling, we conducted multiple tests. To verify input voltage effects, we operated the oil-jet thruster under various input voltages: 10V, 10.5V, 11V, 11.5V, 12V. To verify control voltage effects, we operated the thruster under various control voltages, which change by 0.1V increments in the range of 0.7-3.5V. The measurement error was reduced by calculating the average value.

Fig.11 shows the result of the thruster force versus control voltage under various input voltages. The results indicate that the thruster force will increase as the control voltage increases. When the control voltage is above 3.2V, the thrust of thruster will increase as the input voltage increases. The maximum thruster force is 0.63N under the control voltage of 3.2V and the input voltage of 12V.

The battery voltage range of robot is approximately 11-12V. We use the data fitting method to get the relationship between the thruster force and control voltage under the input voltage 11.5V, as shown in Equation (18).

$$F = 0.0586U^2 + 0.0029U - 0.0215 \quad (18)$$

where, F is the thruster force of oil-jet thruster, U is the control voltage.

V. CONTROLLER DESIGN

A. DECOUPLED DYNAMICS MODEL OF THE SSTIR

When AUV moves at low speed, the equation of motion can be divided into three non-interacting subsystems, including the speed system, the steering subsystem, and the diving subsystem [32]. Since this paper researches the control method for the robot hovering, we only focus on the diving subsystem and the steering subsystem of the robot. In the diving system, the decoupled depth dynamics model of the robot can be simplified as,

$$\begin{cases} \dot{Z} = w \\ (m - Z_{\dot{w}})\,\dot{w} + \left(Z_w + Z_{w|w|}\,|w|\right) w \\ = F_w + B - M + W_w \end{cases} \quad (19)$$

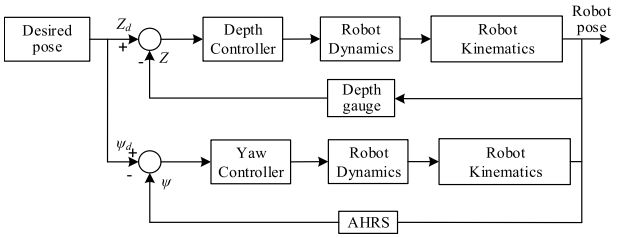

FIGURE 12. The block diagram of the cascade control system.

In the steering system, the decoupled yaw dynamics model of the robot can be simplified as,

$$\begin{cases} \dot{\psi} = r \\ (I_z - N_{\dot{r}})\,\dot{r} + \left(N_r + N_{r|r|}\,|r|\right) r = T_r + W_r \end{cases} \tag{20}$$

The hovering control of the SSTIR is that the robot can dive to the desired depth, and rotate to the desired yaw angle. Consequently, the depth control moves the robot to desired depth at first. Once the robot stays at the target depth, the yaw control will be activated. Fig.12 shows the block diagram of the cascade control system.

B. DEPTH CONTROL SYSTEM DESIGN

Based on the decoupled depth dynamics model of the robot, we put forward block diagram of depth control system, as shown in Fig.13. The depth gauge feeds back depth information during the depth control. Depth control system consists of self-learning controller and adaptive sliding mode backstepping controller.

1) SELF-LEARNING CONTROLLER

The positive buoyancy mainly depends on the density of transformer oil. Transformer oil is aging for long-time high temperature and voltage transformer environment [38]. The Oil aging will change its density. Therefore, the positive buoyancy cannot be obtained by theoretical calculations.

We design self-learning controller to get the control voltage of oil-jet thruster F_d, whose thrust will counteract the positive buoyancy of the SSTIR. The flow diagrams of self-learning controller are shown in Fig. 14, where F is the increase voltage, k is the proportional constant, Z_d is the desired depth of the robot is Z_d, Z is the present depth of the robot, ΔZ is the depth threshold, and n is the thrust threshold.

2) ADAPTIVE SLIDING MODE BACKSTEPPING CONTROL

The control voltage of oil-jet thruster F_d can counteract the positive buoyancy of the SSTIR. The positive buoyancy should be neglected in designing a depth controller. Equation (19) can be further simplified as,

$$\begin{cases} \dot{Z} = w \\ \dot{w} = A_w w + B_w F_w + W_w \end{cases} \tag{21}$$

where $A_w = -\frac{(Z_w + Z_{w|w|}|w|)}{m - Z_{\dot{w}}}$, $B_w = \frac{1}{m - Z_{\dot{w}}}$. W_w is a disturbance force vector, $|W_w| < \delta$, $\dot{W}_w = 0$.

Suppose the desired depth of the robot is Z_d, the present depth of the robot is Z. Define a depth error vector,

$$z_1 = Z - Z_d \tag{22}$$

Invoking (21) with (22) yields,

$$\dot{z}_1 = \dot{Z} - \dot{Z}_d = w - \dot{Z}_d \tag{23}$$

A Lyapunov function candidate can be chosen as,

$$V_1 = \frac{1}{2} z_1^2 \tag{24}$$

Define, $w = z_2 + \dot{Z}_d - c_1 z_1$, where, $c_1 > 0$ is a positive constant, $z_2 = w - \dot{Z}_d + c_1 z_1$ is virtual control vector. Equation (23) can be written as,

$$\dot{z}_1 = z_2 - c_1 z_1 \tag{25}$$

Differentiating the Lyapunov function (24),

$$\dot{V}_1 = z_1 \dot{z}_1 = z_1 z_2 - c_1 z_1^2 \tag{26}$$

Define the switching function, $\sigma = k_1 z_1 + z_2$, where $k_1 > 0$ is a positive constant. Invoking (25) with the switching function yields,

$$\sigma_w = k_1 z_1 + z_2 = (k_1 + c_1)\, z_1 + \dot{z}_1 \tag{27}$$

Since, $k_1 + c_1 > 0$, if $\sigma_w = o$, then, $z_1 = 0$, $z_2 = 0$, and $\dot{V}_1 \le 0$.

A Lyapunov function candidate for depth control can be chosen as,

$$V_2 = V_1 + \frac{1}{2}\sigma_w^2 + \frac{1}{2r}\widetilde{W}_w^2 \tag{28}$$

where, $\widetilde{W}_w$ is disturbance-tracking error, which is defined to be $\widetilde{W}_w = W_w - \widehat{W}_w$, $\widehat{W}_w$ is the estimated disturbance vector, $\gamma > 0$ is a positive constant.

Then,

$$\begin{aligned} \dot{V}_2 &= \dot{V}_1 + \sigma\dot{\sigma} + \frac{1}{\gamma}\widetilde{W}_w\dot{\widetilde{W}}_w \\ &= z_1 z_2 - c_1 z_1^2 + \sigma_w\left(k_1 \dot{z}_1 + \dot{z}_2\right) - \frac{1}{\gamma}\widetilde{W}_w\dot{\widehat{W}}_w \\ &= z_1 z_2 - c_1 z_1^2 + \sigma_w\left(k_1\left(z_2 - c_1 z_1\right) + \dot{w} - \ddot{Z}_d + c_1\dot{z}_1\right) \\ &\quad - \frac{1}{\gamma}\widetilde{W}_w\dot{\widehat{W}}_w \\ &= z_1 z_2 - c_1 z_1^2 + \sigma_w\left(k_1\left(z_2 - c_1 z_1\right) + B_w F_w + \widehat{W}_w\right. \\ &\quad + A_w\left(\dot{z}_2 + \dot{Z}_d - c_1 z_1\right) \\ &\quad \left. - \ddot{Z}_d + c_1\dot{z}_1\right) - \frac{1}{\gamma}\widetilde{W}_w\left(\dot{\widehat{W}}_w + \gamma\sigma_w\right) \end{aligned} \tag{29}$$

The adaptive sliding mode backstepping controller can be written as,

$$\begin{aligned} F_w = B_w^{-1}\left(-k_1\left(z_2 - c_1 z_1\right) - A_w\left(\dot{z}_2 + \dot{Z}_d - c_1 z_1\right)\right. \\ \left. - \widehat{W}_w + \ddot{Z}_d - c_1\dot{z}_1 - h_w\left(\sigma_w + \beta_w sgn\left(\sigma_w\right)\right)\right) \end{aligned} \tag{30}$$

where, $h_w > 0, \beta_w > 0$.

The adaptive law for the controller is,

$$\dot{\widehat{W}}_w = -\gamma\sigma \tag{31}$$

3) STABILITY ANALYSIS

Invoking (30) and (31) with (29) yields,

$$\dot{V}_2 = z_1 z_2 - c_1 z_1^2 - h_w \sigma^2 - h_w \beta_w |\sigma| \tag{32}$$

Define, $Q = \begin{bmatrix} c_1 + h_w k_1^2 & h_w k_1 - \frac{1}{2} \\ h_w k_1 - \frac{1}{2} & h_w \end{bmatrix}$, then,

$$\begin{aligned} z^T Q z &= \begin{bmatrix} z_1 & z_2 \end{bmatrix} \begin{bmatrix} c_1 + h_w k_1^2 & h_w k_1 - \frac{1}{2} \\ h_w k_1 - \frac{1}{2} & h_w \end{bmatrix} \begin{bmatrix} z_1 & z_2 \end{bmatrix}^T \\ &= c_1 z_1^2 - z_1 z_2 + h_w k_1^2 z_1^2 + 2 h_w k_1 z_1 z_2 + h_w z_2^2 \\ &= c_1 z_1^2 - z_1 z_2 + h_w \sigma^2 \end{aligned} \tag{33}$$

The determinant of matrix Q can be written as,

$$\begin{aligned} |Q| &= h_w \left(c_1 + h_w k_1^2 \right) - \left(h_w k_1 - \frac{1}{2} \right)^2 \\ &= h_w \left(c_1 + k_1 \right) - \frac{1}{4} > 0 \end{aligned} \tag{34}$$

Invoking (33) with (32) yields,

$$\dot{V}_2 = -z^T Q z - h_w \beta_w |\sigma| \leq 0 \tag{35}$$

We can choose the design parameter h_w, c_1 and k_1, satisfying the inequality (34). *If* Q is positive definite matrix, the inequality (35) is true. Then the stability of the controller is guaranteed.

C. YAW CONTROL SYSTEM DESIGN

For designing controller, Equation (20) can be written as,

$$\begin{cases} \dot{\psi} = r \\ \dot{r} = A_r r + B_r T_r + W_r \end{cases} \tag{36}$$

where, $A_r = -\frac{(N_r + N_{r|r|}|r|)}{I_z - N_{\dot{r}}}$, $B_r = \frac{1}{I_z - N_{\dot{r}}}$, $W_r = \frac{W}{I_z - N_{\dot{r}}}$, W_r is a disturbance force vector, $|W_r| < \mu$, $\dot{W}_r = 0$.

Referring to design process of the depth controller, the yaw controller of sliding mode backstepping can be written as,

$$\begin{aligned} T_{\psi b} = B_r^{-1} \big(& -k_2 (\psi_2 - c_3 \psi_1) - A_r \left(\dot{\psi}_2 + \dot{\psi}_d - c_3 \psi_1 \right) \\ & - usgn(s) + \ddot{\psi}_d - c_3 \dot{\psi}_1 - h_r \left(\sigma_r + \beta_r sgn\left(\sigma_r \right) \right) \big) \end{aligned} \tag{37}$$

where, ψ_d is a desired yaw of the robot, ψ is the present yaw of the robot. k_2, c_3, h_r, σ_r are positive constant, respectively. Define a depth error vector $\psi_1 = \psi - \psi_d$. Define virtual control vector, $\psi_2 = r - \dot{\psi}_d + c_3 \psi_1$, Define the switching function, $\sigma_r = k_2 \psi_1 + \psi_2$.

VI. SIMULATION STUDIES

Simulation experiments were carried out to verify the effectiveness of the proposed method. The hydrodynamic parameters of the SSTIR dynamic model are shown in Table 1. There are two scenarios used for testing hover-style control of robot: depth control in vertical plane, and yaw control in horizontal plane.

TABLE 1. Parameters of the SSTIR dynamics model.

m	3.274kg	I_z	0.01kgm^2		
$Z_{\dot{w}}$	-7.63×10^{-3}kg	Z_w	-6.82×10^{-3}kg/s	$Z_{w\|w\|}$	-6.21×10^{-3}kg/s
$N_{\dot{r}}$	-4.33×10^{-5} kg	N_r	-4.11×10^{-5}kg/s	$N_{r\|r\|}$	-2.09×10^{-4}kg/s

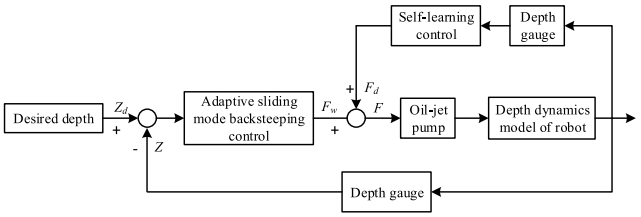

FIGURE 13. The block diagram of depth control system.

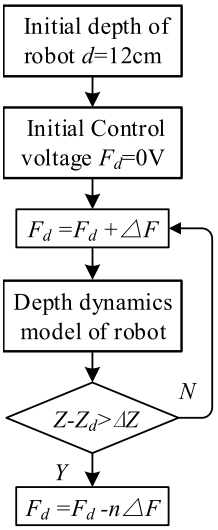

FIGURE 14. The flow diagrams of self-learning controller.

A. DEPTH CONTROL IN VERTICAL PLANE

The Self-learning controller parameters are given directly in the simulation experiments. The adaptive sliding mode backstepping controller is given by Equation (30). The depth of the robot starts from the surface, and is programmed with four consecutive depth demands of 1.5, 2, 1.5 and 1m. The contrasts between single neuron PID controller and adaptive sliding mode backstepping controller in the depth control are shown in Fig. 15 and 16. The contrasts of depth control results are shown in Fig. 15, where the black dotted line is the desired depth, the blue solid line is the control result with ASMBC controller, the red solid line is the control result with SN-PID controller. As shown in Fig. 15, the setting time of ASMBC is only 22s, which is smaller than SN-PID. The overshoot of ASMBC is smaller than SN-PID. The maximum deviation of ASMBC is 4cm. Since the robot moves in upward direction by positively buoyant, the ASMBC value is the same as the SN-PID value during the upward movement of robot. The disturbance appeases at the time = 100s, the ASMBC could restore the system to a stable state. The contrasts of velocity

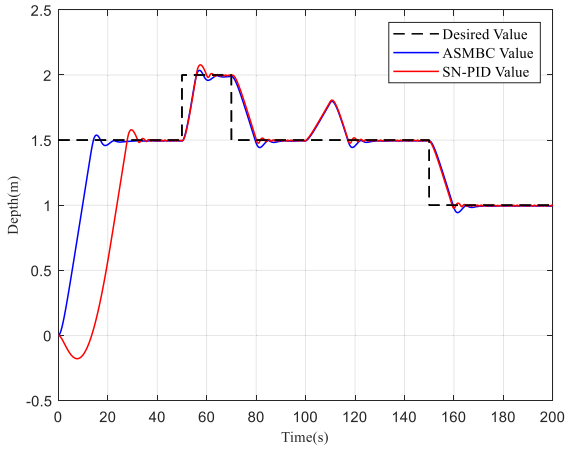

FIGURE 15. Depth control results in the simulation experiments.

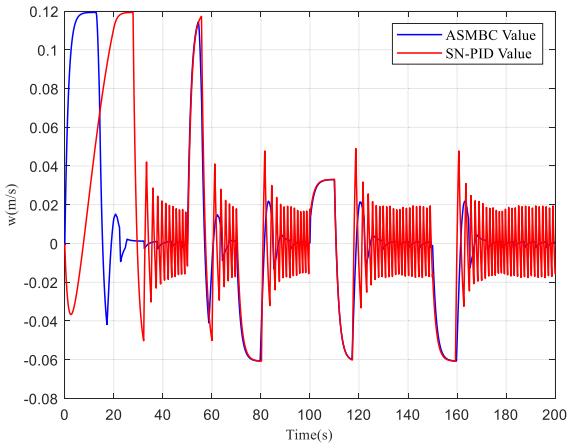

FIGURE 16. Vertical speed control results in the simulation experiments.

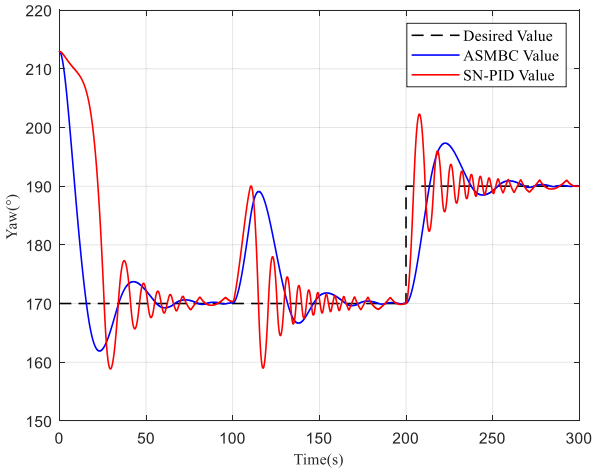

FIGURE 17. Yaw control results in the simulation experiments.

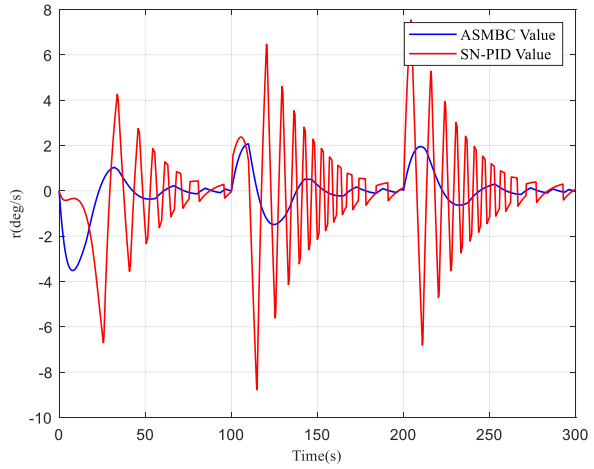

FIGURE 18. Rotating speed control results in the simulation experiments.

control results are shown in Fig.16, where the blue solid line is the control result with ASMBC controller, the red solid line is the control result with SN-PID controller. The velocity of ASMBC is smaller than SN-PID in the steady state. As shown in Fig. 15 and 16, with consideration of the overshoot, the setting time, and the steady state, the ASMBC controller is obviously superior to the SN-PID.

B. YAW CONTROL IN HORIZONTAL PLANE

The adaptive sliding mode backstepping controller for yaw is given by Equation (37). The initial yaw angle of the robot is 210°, with the desired yaw angle of 170° and 190°. The performance of the ASMBC controller is compared to the SN-PID controller. The contrasts of yaw control results are shown in Fig.17, where the black dotted line is the desired yaw, the blue solid line is the control result with ASMBC controller, red solid line is the control result with SN-PID controller. As shown in Fig. 17, the convergence speed of ASMBC was faster than SN-PID controller. The maximum deviation of ASMBC is 8°, which is smaller than SN-PID. There hardy existed overshoot in the steady state. The maximum deviation of ASMBC is within 2 degrees in the steady state. The disturbance appears at the time = 100s, the ASMBC could restore the system to a stable state. The contrasts of velocity control results are shown in Fig. 18, where the blue solid line is the control result with ASMBC controller, the red solid line is the control result with SN-PID controller. The robot moves smoothly with ASMBC controller. As shown in Fig. 17 and 18, with consideration of the overshoot, convergence speed, and the steady state, the ASMBC controller is a more reliable controller with a better performance.

VII. RESULTS OF TRANSFORMER OIL TANK EXPERIMENTS

To examine the performance of ASMBC controller, the tank experiments was carried out at Shenyang Institute of Automation, Chinese Academy of Sciences in a with the dimensions of 120cm*80cm*80cm. The transformer oil tank is shown in Fig. 19.

The depth controller parameters are set as follows, $F = 0.1$V, $\Delta Z = 5$cm, $n = 4$, $h_w = 4.9$, $\beta_w = 1.2$,

FIGURE 19. The transformer oil tank.

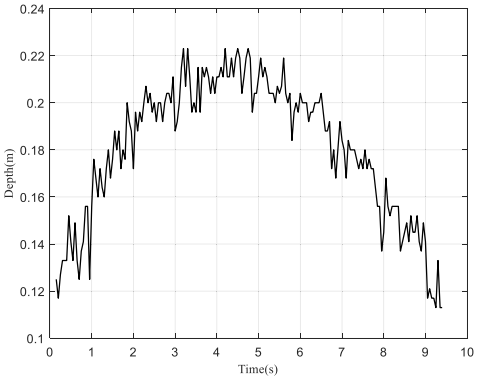

FIGURE 20. Self-learning control results in the oil tank.

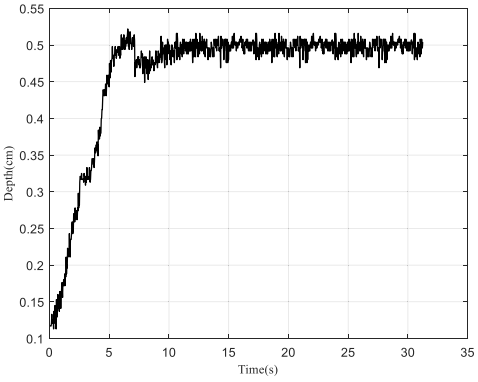

FIGURE 21. Depth control results in the oil tank.

$c_1 = 4.83$, $k_1 = 28.6$. The yaw controller parameters are set as follows, $h_r = 15$, $\beta_r = 0.4$, $c_3 = 0.1$, $k_2 = 56.3$.

The initial depth of the robot is 0.12m, with the desired depth of 50cm. The initial yaw angle of the robot is 2°, with the desired yaw angle of 150°. The depth control results are shown in Fig. 20 and 21. As shown in Fig. 20, self-learning controller is carried out to obtain F_d at first. Then, the depth controller with the Equation (30) starts to control movement in vertical plane. The maximum deviation is within 1cm in the steady state. The performance of the depth control is satisfactory, as the overshoot, the setting time state steady state are small. The results of yaw control are shown in Fig. 22.

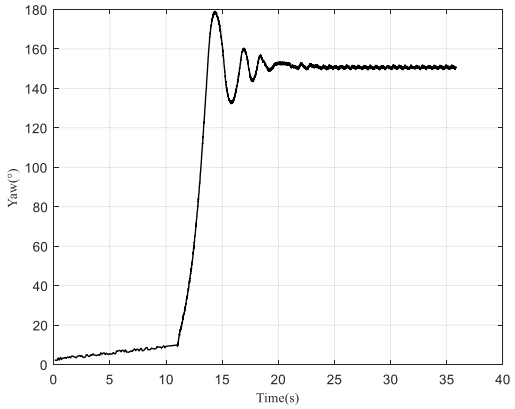

FIGURE 22. Yaw control results in the oil tank.

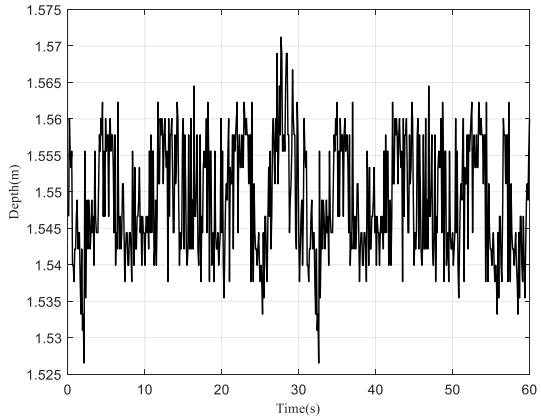

FIGURE 23. Depth control results in the 220kV transformer.

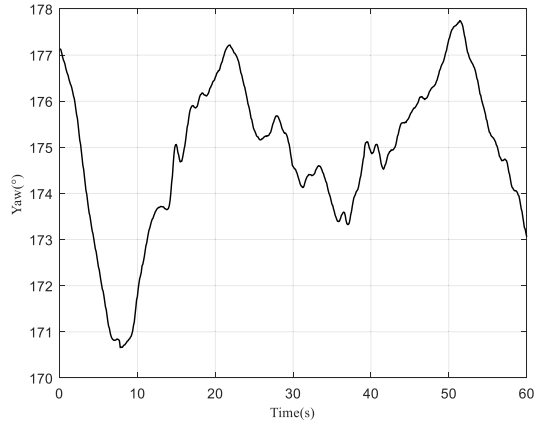

FIGURE 24. Yaw control results in the 220kV transformer.

It can be seen from the results that the robot rotates slowly in the yaw direction during the depth control process. After the depth control of the robot is stable, the yaw control of the SSTIR will be activated at time = 11s. The maximum deviation of ASMBC is within 2 degrees in the steady state. The control precision can satisfy the requirement of fault observation tasks.

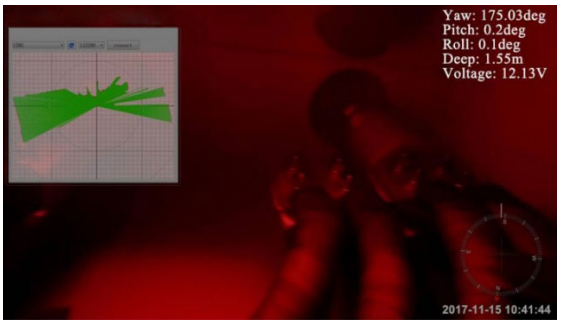

FIGURE 25. Video image of the robot.

On the basis of the oil tank test, the SSTIR entered into the 220kV Mitsubishi transformer, and carried out application test. The SSTIR enters the transformer through the manhole on the top of the transformer. The robot works at a depth of 1.55 meters and a yaw angle of 175° for 1 minute. The results of the experiments are shown in Fig. 23 and 24. The maximum deviation of depth is within 3 centimeters in the steady state. The maximum deviation of yaw angle is within 4 degrees in the steady state.

The robot control terminal receives video image, which is shown in Fig. 25. Video image can be used to determine whether there is a fault in the transformer.

VIII. CONCLUSION

A new spherical submersible transformer inspection robot is designed for the problem of locating and identifying the faults of oil-immersed transformers in this paper. The shape structure of the robot is spherical which has a zero turning radius with multi-degree of freedom movements. The movement of the spherical robot is susceptible to external distracters. The cascade control system based on the ASMBC is put forward for hovering control of the spherical robot. Both simulation experiments and real trials were carried out to verify the performance of the design controller. The results of transformer application tests show that the robot can take the place of the manual inspection to complete the fault detection tasks. Hovering control is the basis for autonomous observation of robot in the oil-immersed transformer. In the future, we will focus on the three-dimensional optimal path planning and tracking control of the robot

REFERENCES

[1] S. Shahabi, M. Mirzaei, A. Gholami, and S. Taheri, "Investigation of performance of ferroresonance suppressing circuits in coupling capacitor voltage transformers," in *Proc. 4th IEEE Conf. Ind. Electron. Appl.*, Xi'an, China, May 2009, pp. 216–221.

[2] K. Pourhossein, G. B. Gharehpetian, E. Rahimpour, and B. N. Araabi, "A probabilistic feature to determine type and extent of winding mechanical defects in power transformers," *Electr. Power Syst. Res.*, vol. 82, no. 1, pp. 1–10, Jan. 2012.

[3] C. T. Dervos, C. D. Paraskevas, P. D. Skafidas, and N. Stefanou, "Dielectric spectroscopy and gas chromatography methods applied on high-voltage transformer oils," *IEEE Trans. Dielectr. Electr. Insul.*, vol. 13, no. 3, pp. 586–592, Jun. 2006.

[4] A. J. R. Reis, L. G. Castanheira, and R. C. Barbosa, "Enhancing neural networks-based classification of incipient faults in power transformers via preprocessing," in *Proc. BRICS Congr. Comput. Intell. 11th Brazilian Congr. Comput. Intell.*, Ipojuca, Brazil, Sep. 2013, pp. 622–627.

[5] J. Jiang, G. Ma, H.-T. Song, C. Li, H.-M. Zhan, H.-B. Wang, and Y.-T. Luo, "Dissolved acetylene detection in power transformer oil based on near-infrared absorption spectrum method," in *Proc. IEEE Conf. Electr. Insul. Dielectr. Phenomena (CEIDP)*, Ann Arbor, MI, USA, Oct. 2015, pp. 43–46.

[6] A. Y. Arabul and I. Senol, "Development of a hot-spot temperature calculation method for the loss of life estimation of an ONAN distribution transformer," *Electr. Eng.*, vol. 100, no. 3, pp. 1651–1659, Sep. 2018.

[7] K. Zhang, F. Yuan, J. Guo, and G. Wang, "A novel neural network approach to transformer fault diagnosis based on momentum-embedded BP neural network optimized by genetic algorithm and fuzzy c-means," *Arabian J. Sci. Eng.*, vol. 41, no. 9, pp. 3451–3461, Sep. 2016.

[8] M. Žarković and Z. Stojković, "Analysis of artificial intelligence expert systems for power transformer condition monitoring and diagnostics," *Electr. Power Syst. Res.*, vol. 149, pp. 125–136, Aug. 2017.

[9] K. Bacha, S. Souahlia, and M. Gossa, "Power transformer fault diagnosis based on dissolved gas analysis by support vector machine," *Electr. Power Syst. Res.*, vol. 83, no. 1, pp. 73–79, Feb. 2012.

[10] J. Nosratian Ahour, S. Seyedtabaii, and G. B. Gharehpetian, "Determination and localisation of turn-to-turn fault in transformer winding using frequency response analysis," *IET Sci., Meas. Technol.*, vol. 12, no. 3, pp. 291–300, May 2018.

[11] G. C. H. Shah. ABB Ability Inspection for Transformers-TXplore. ABB USCRC Mechatronics Sensors Bloomfield, CT, USA. Accessed: Aug. 23, 2018. [Online]. Available: https://new.abb.com/products/transformers/s-ervice/advanced-services/txplore

[12] G. C. H. Shah, C. Stiegemeier, and J. Stapleton. ABB TXplore Robot Redefines Transformer Inspection-Transformer in Renewables Application-ABB Special Report Transformers. ABB, USA. Accessed: Oct. 19, 2018. [Online]. Available: https://new.abb.com/products/transformers/s-ervice/advanced-services/txplore

[13] V. A. Panov, Y. M. Kulikov, E. E. Son, A. S. Tyuftyaev, M. K. Gadzhiev, and P. L. Akimov, "Electrical breakdown voltage of transformer oil with gas bubbles," *High Temp.*, vol. 52, no. 5, pp. 770–773, Sep. 2014.

[14] B. K. Sahu and B. Subudhi, "The state of art of autonomous underwater vehicles in current and future decades," in *Proc. 1st Int. Conf. Autom., Control, Energy Syst. (ACES)*, Feb. 2014, pp. 1–6.

[15] K. Tanakitkorn, P. A. Wilson, S. R. Turnock, and A. B. Phillips, "Depth control for an over-actuated, hover-capable autonomous underwater vehicle with experimental verification," *Mechatronics*, vol. 41, pp. 67–81, Feb. 2017.

[16] G. Antonelli, S. Chiaverini, N. Sarkar, and M. West, "Adaptive control of an autonomous underwater vehicle: Experimental results on ODIN," *IEEE Trans. Control Syst. Technol.*, vol. 9, no. 5, pp. 756–765, Sep. 2001.

[17] H. T. Choi, A. Hanai, S. K. Choi, and J. Yuh, "Development of an underwater robot, ODIN-III," in *Proc. IEEE/RSJ Int. Conf. Intell. Robots Syst. (IROS)*, Las Vegas, NV, USA, Oct. 2003, pp. 836–841.

[18] X. Lan, H. Sun, and Q. Jia, "Principle and dynamic analysis of a new-type spherical underwater vehicle," *J. Beijing Univ. Posts Telecommun.*, vol. 33, no. 3, pp. 20–23, 2010.

[19] H. Sun, "Dynamic model of the BYQ-3 spherical robot," *J. Mech. Eng.*, vol. 45, no. 10, pp. 8–14, 2009.

[20] Z. Liu, H. Sun, Y. Li, Q. Jia, and M. Chu, "Finite time point-stabilization of underwater spherical roving robot," *J. Vibroeng.*, vol. 18, no. 6, pp. 3719–3733, Sep. 2016.

[21] C. Yue, S. Guo, M. Li, Y. Li, H. Hirata, and H. Ishihara, "Mechatronic system and experiments of a spherical underwater robot: SUR-II," *J. Intell. Robot. Syst.*, vol. 80, no. 2, pp. 325–340, Nov. 2015.

[22] S. Gu and S. Guo, "Performance evaluation of a novel propulsion system for the spherical underwater robot (SURIII)," *Appl. Sci.*, vol. 7, no. 11, pp. 1196–1201, 2017.

[23] I. C. Rust and H. H. Asada, "The eyeball ROV: Design and control of a spherical underwater vehicle steered by an internal eccentric mass," *Nelineinaya Dinamika*, vol. 10, no. 4, pp. 513–531, 2014.

[24] Y. He, L. Zhu, G. Sun, and M. Dong, "Underwater autonomous motion control of a small-scaled spherical robot with neural networks," *Microsyst. Technol.*, vol. 25, no. 4, pp. 1297–1309, Apr. 2019.

[25] L. V. Steenson, "Experimentally verified model predictive control of a hover-capable AUV," Ph.D. dissertation, Univ. Southampton, Southampton, U.K., 2013.

[26] A. Alvarez, A. Caffaz, A. Caiti, G. Casalino, L. Gualdesi, A. Turetta, and R. Viviani, "Folaga: A low-cost autonomous underwater vehicle combining glider and AUV capabilities," *Ocean Eng.*, vol. 36, no. 1, pp. 24–38, Jan. 2009.

[27] E. You Hong, H. Geok Soon, and M. Chitre, "Depth control of an autonomous underwater vehicle, STARFISH," in *Proc. IEEE OCEANS*, Sydney, NSW, Australia, May 2010, pp. 1–6.
[28] T. A. Prevost and T. V. Oommen, "Cellulose insulation in oil-filled power transformers: Part I—History and development," *IEEE Elect. Insul. Mag.*, vol. 22, no. 1, pp. 28–35, Jan. 2006.
[29] J. T. Bendler, *Handbook of Polycarbonate Science and Technology*. New York, NY, USA: CRC Press, 1999, pp. 56–64.
[30] J. Kim and W. K. Chung, "Accurate and practical thruster modeling for underwater vehicles," *Ocean Eng.*, vol. 33, nos. 5–6, pp. 566–586, Apr. 2006.
[31] S. B. Chandanapalli, "Design and deployment of Aqua monitoring system using wireless sensor networks and IAR-kick," *J. Aquaculture Res. Develop.*, vol. 5, no. 7, pp. 1–10, 2014.
[32] I. T. Fossen, *Guidance and Control of Ocean Vehicles*. New York, NY, USA: Wiley, 1994, pp. 35–58.
[33] P. Ridao, J. Batlle, and M. Carreras, "Dynamics model of an underwater robotic vehicle," Inst. Informat. Appl., Univ. Girona, Girona, Spain, 2001, pp. 3–28.
[34] B. Prasad, A. Agrawal, V. Viswanathan, A. R. Chowdhury, R. Kumar, and S. K. Panda, "A visually guided spherical underwater robot," in *Proc. IEEE Underwater Technol. (UT)*, Chennai, India, Feb. 2015, pp. 1–6.
[35] M. Ataei and A. Yousefi-Koma, "Three-dimensional optimal path planning for waypoint guidance of an autonomous underwater vehicle," *Robot. Auto. Syst.*, vol. 67, pp. 23–32, May 2015.
[36] J. Kim, H. Joe, S.-C. Yu, J. S. Lee, and M. Kim, "Time-delay controller design for position control of autonomous underwater vehicle under disturbances," *IEEE Trans. Ind. Electron.*, vol. 63, no. 2, pp. 1052–1061, Feb. 2016.
[37] X. Lin, S. Guo, K. Tanaka, and S. Hata, "Underwater experiments of a water-jet-based spherical underwater robot," in *Proc. IEEE Int. Conf. Mechatronics Autom.*, Beijing, China, Aug. 2011, pp. 738–742.
[38] E. M. M. El-refaie, M. R. Salem, and W. A. Ahmed, "Prediction of the characteristics of transformer oil under different operation conditions," *World Acad. Sci., Eng. Technol.*, vol. 53, pp. 764–768, May 2009.

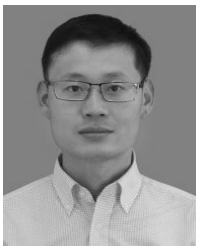

YINGBIN FENG received the B.S. degree in measurement and control technology and instrumentation from Shenyang Ligong University, Shenyang, China, in 2009, and the Ph.D. degree in pattern recognition and intelligent system from the Shenyang Institute of Automation, Chinese Academy of Sciences, Shenyang, China, in 2015. He is currently an Assistant Professor at the Shenyang Ligong University. His research interests include underwater vehicles design, modeling, and control.

YANJU LIU received the B.S. degree from the Department of Electrical Engineering, Shenyang University of Technology, Shenyang, China, in 1987, the M.S. degree in automation from Northeastern University, in 1996, and the Ph.D. degree in electrical engineering from the Shenyang University of Technology, in 2011. She is currently a Full Professor at Shenyng Ligong Univerity. Her research forcuses on robot vision and target recognition.

HONGWEI GAO received the Ph.D. degree in pattern recognition and intelligent system from the Shenyang Institute of Automation (SIA), Chinese Academy of Sciences (CAS), in 2007. Since September 2015, he has been a Professor with the School of Automation and Electrical Engineering, Shenyang Ligong University. He is currently the leader of the academic direction for optical and electrical measuring technology and systems. His research interests include digital image processing and analysis, stereo vision, and intelligent computation. He has published more than 60 technical articles in these areas as a first author or coauthor.

ZHAOJIE JU (Senior Member, IEEE) received the B.S. degree in automatic control and the M.S. degree in intelligent robotics from the Huazhong University of Science and Technology, China, and the Ph.D. degree in intelligent robotics from the University of Portsmouth, U.K. He held research appointments at University College London, London, U.K., before he started his independent academic position at the University of Portsmouth, in 2012. He has authored or coauthored over 180 publications in journals, book chapters, and conference proceedings. His research interests include machine intelligence, pattern recognition and their applications on human motion analysis, multifingered robotic hand control, human–robot interaction and collaboration, and robot skill learning. He received the four best paper awards and the one best AE award in ICRA2018.